Status of the performance of the Euclid spacecraft

Luis M. Gaspar Venancio*[a], Lionel Carminati [b], Jérôme Amiaux[c], Luciana Bonino[d], Giuseppe Racca[a], Roland Vavrek[a], René Laureijs[a], Alex Short[a], Tobias Boenke[a], Paolo Strada[a]

[a]European Space Agency, ESTEC, Keplerlaan 1, 2201 AZ Noordwijk, +31 (0) 71; [b]Airbus Defence&Space, 31 rue des Cosmonautes, Z.I. du Palays, 31402 Toulouse Cedex 4, France; [c]CEA/Service d'Astrophysique, Orme des Merisiers Bat.109, 91191 Gif sur Yvette, France; [d]Thales Alenia Space Italia, Strada Antica di Collegno, 10146 Torino, Italy

ABSTRACT

The Euclid mission, of which the spacecraft is the essential space segment, is being developed to undertake the challenges of mapping the dark energy and dark matter distribution in the Universe. As the launch date is approaching (2nd half of 2022), the development of the spacecraft has successfully passed critical milestones with the manufacturing and integration of the telescope, instruments and service module. Each sub-element of the spacecraft has been qualified and their performance assessed. The assembly of the complete payload and spacecraft is currently on-going. The integrated optical performance end to end of the payload module is currently being assessed based on the as-built knowledge of the parts of the telescope and instruments.

Keywords: Euclid, payload, development, performance

1. INTRODUCTION

Euclid is a high-precision survey mission designed to map the distribution of dark matter and investigate the nature of the dark energy in the Universe. The mission will implement two probes: Weak Lensing (WL) and Galaxy Clustering (GC) that is used to investigate Baryonic Acoustic Oscillations (BAO). These probes require a high image quality, near-infrared spectroscopic and optical imaging capabilities and very high system stability to minimize systematic effects. The probes require the observation of tens of millions to two billions of galaxies over a sky area covering 15000 deg^2. Such mission constraints[1] are directly translated in the design and manufacturing of the space segment of the mission[2].

The Euclid's space segments consists of a single spacecraft divided in two main modules: the service module (SVM) and the Payload Module (PLM), both represented in Figure 1. The SVM provides the interface of the spacecraft with the launcher and includes all the necessary components and equipment for communication with ground stations, attitude and orbit control (AOCS), data management, instrument command electronics and electric power generation, control and distribution. A sunshield, yielding also solar cells for electrical power generation, protects the PLM from direct sunlight illumination to ensure its thermal stability. Whilst the detailed design and architecture of the PLM is described elsewhere[3], its main characteristics are reminded hereafter. The PLM, interfacing with the SVM as shown in Figure 1, comprises a 1.2-m class Korsch-type telescope directing the incoming light towards two separated instruments: the VISible imager(VIS)[4] and the Near-Infrared Spectrometer & Photometer(NISP)[5][6]. The main optical requirements of the mission and instruments are recalled in Table 1. The telescope structure and its mirrors are made out of Silicon Carbide (SiC) to optimize the stability against thermal perturbations of the image quality delivered to the instruments. The telescope has a refocusing and tip/tilt capability implemented on the secondary mirror to compensate for any drift in the image quality during the mission.

The spacecraft subsystems passed successfully their Critical Design Review (CDR). This paper intends, in the first part, to report on the current status of the development of the different sub-systems of the Euclid spacecraft. The second part of the paper will report on the performance end to end of the PLM updated with, when available, measurements performed on manufactured elements.

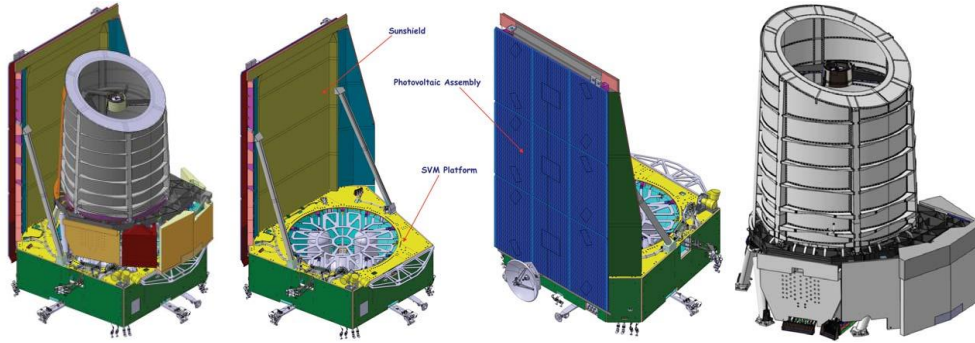*luis.miguel.gaspar.venancio@esa.int; phone +31 (0) 71 565 8054; www.esa.int

Figure 1. Euclid spacecraft overview. From left to right: spacecraft with SVM and PLM integrated; front view of the SVM; back view of the SVM; overview of the integrated PLM.

SURVEYS					
Wide survey	deg2	15000	Step and stare with 4 dither pointings per step.		
Deep survey		40	In at least 2 patches of > 10 deg 2 2 magnitudes deeper than wide survey		
PAYLOAD					
Telescope	1.2m Korsch, focal length=24500mm				
Instrument		VIS	NISP		
FoV	deg^2	0.787×0.709	0.763×0.722		
Capability		Imaging	Imaging photometry (NIP)		Spectroscopy (NIS)
Spectral range	nm	550-900	920-1192	1192-1544	1544-2000	920-1300, 1200-1850
Plate scale	arcsec/pixel	0.1	0.3		
Resolving power		Not applicable	Not applicable		380
Sensitivity		$m_{AB} = 24.5$	$m_{AB} = 24$		$6×10^{-17}, 2×10^{-16}$ erg.cm^{-2}.s^{-1}
Detector technology		36 arrays 4k×4k CCD	16 arrays 2k×2k NIR sensitive HgCdTe detectors		
SPACECRAFT					
Launcher	Soyuz ST-2.1 B from Kourou				
Orbit	Large Sun-Earth Lagrange point 2 (SEL2), free insertion orbit				
Pointing	75 mas relative pointing error over one dither duration				
Observation mode	Step and stare, 4 dither frames per field, VIS and NISP common FoV = 0.54 deg 2				
Lifetime	6.5 years				

Table 1. Mission and spacecraft main design driving requirements

2. SPACECRAFT DEVELOPMENT STATUS

2.1 Service module

The development of the SVM and of the Euclid's spacecraft is under the responsibility of Thales Alenia Space Italia (TAS-I). The SVM contains all the elements to interface with the PLM and the launcher as well as the equipment necessary for the power generation, control and distribution, the attitude and control, the data handling and communication (Figure 2).
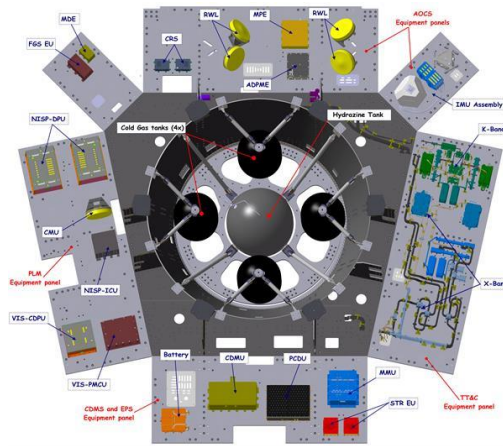

Figure 2. SVM platform internals overview.

The SVM has passed its CDR in 2018 and since then all its elements have been manufactured and are on-going a qualification process. The thermal-mechanical qualification has been completed with the SVM structural model (STM). Many elements have already been integrated after qualification. For instance the propulsion lines are now integrated along with the thrusters and the hydrazine and cold gas tanks are now integrated around the central cone as shown in Figure 3.
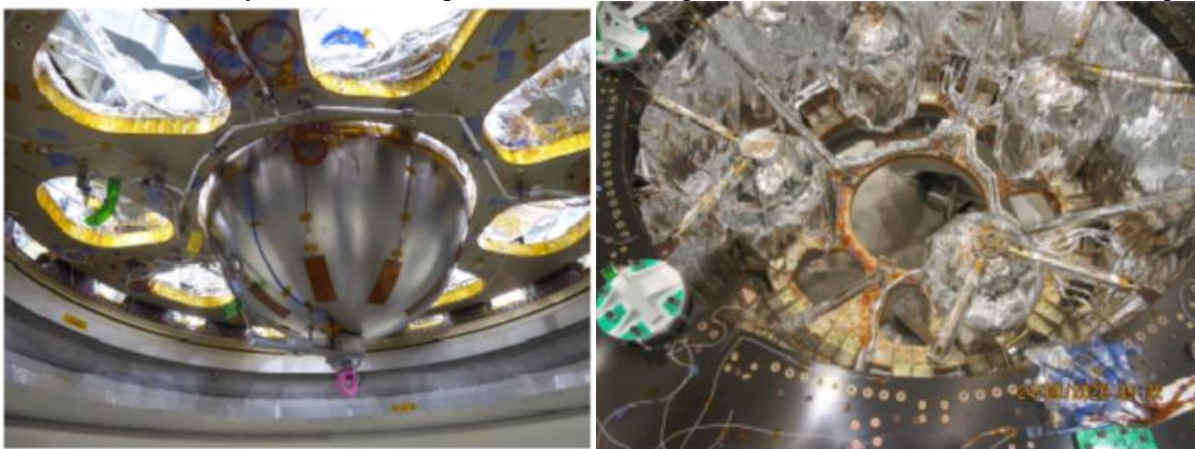

Figure 3. Tanks integrated in the SVM. (Left) Hydrazine tank; (right) cold gas tanks (Courtesy Thales Alenia Space).

All the electronic units have been qualified and delivered for integration on the flight model of the SVM. The integration is performed in a progressive fashion: all units are integrated on lateral panels which electrically tested together before being assembled around the central structure containing also the propulsion systems.

2.2 Payload module

The telescope development and PLM integration is under the responsibility of Airbus Defense & Space (ADS). The instruments are developed under the responsibility of the Euclid Consortium. The development of the VIS instrument is led by the Mullard Space Science Laboratory (MSSL) in the United Kingdom; the development of the NISP instrument is under the responsibility of the Centre Nationale d'Études Spatiales (CNES) in France and led by the Laboratoire d'Astronomie de Marseille.

Telescope

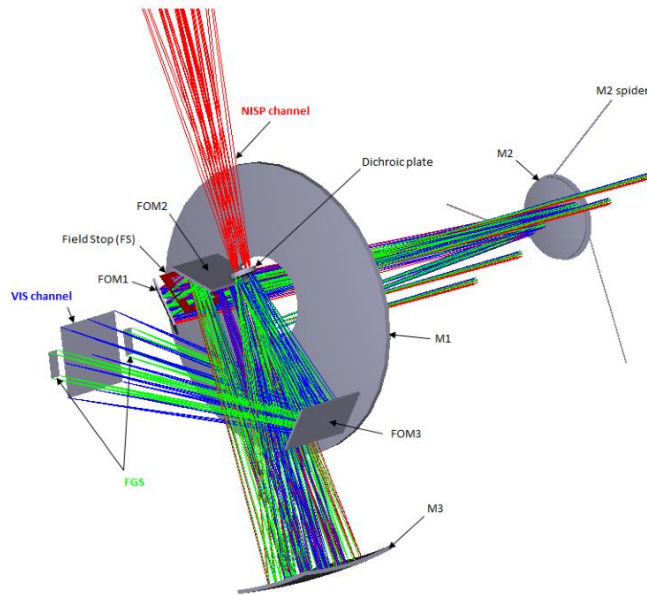The optical layout of the telescope is recalled in Figure 4.

Figure 4. Telescope optical lay-out.

After seven years of development and manufacturing, the flight mirrors and structure of telescope have been integrated on a large baseplate on which the instruments are integrated (Figure 5).
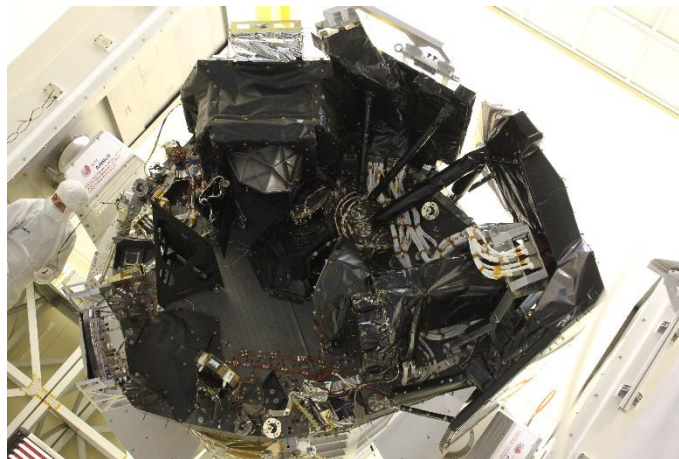

Figure 5. Flight Model (FM) of the PLM showing the implementation of the instruments on the common baseplate (courtesy Airbus Defense&Space). Both instruments units are integrated. The telescope baffle (white vanned part) is mounted, hiding the bi-pods structure supporting the secondary mirror M2.

The telescope alone was optically aligned using a wavefront sensor and its performance verified at room temperature. The following characteristics have been determined:

- The pupil centering at different field points is derived direct imaging of the exit pupil of the telescope. An example of such image is shown in Figure 7. The M2 spider is clearly imaged as well as the mechanical rim of the dichroic so the position of the exit pupil is precisely determined within the reference frame linked to the mechanical rim of the dichroic.

- The field of regard is measured by determining the vignetting function of the telescope. The pupil vignetting is observed as the field is scanned in different directions, allowing to determine the size of the field of view in the scanned direction (Figure 6).

- The wavefront error (WFE) at zero gravity across the field of view using a Shack-Hartmann sensor. The measured WFE amounts to 51.6nmRMS at λ=1064nm, the specification being 60nmRMS.
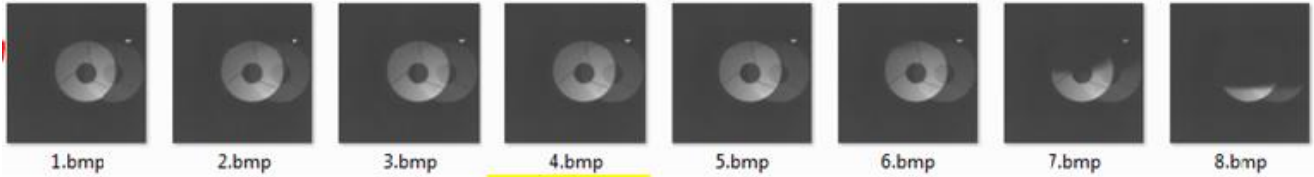

Figure 6. The evolution of the pupil vignetting is clearly visible as the field at the entrance of the telescope is changed.
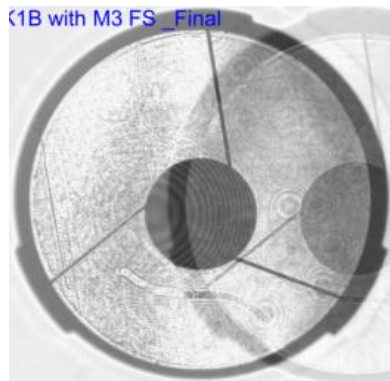

Figure 7. Example of an image of the exit pupil taken at room temperature after alignment of the telescope optical elements.

In addition, the position of the telescope focal plane at room temperature has been precisely determined within the telescope reference frame. Such information, and its associated knowledge error, is crucial for the correct alignment of the instruments with respect to the telescope.

The test campaign at room temperature also included a straylight measurement to verify the compliance of the design to the straylight stringent requirements[7]. For this purpose a dedicated test set-up was implemented (Figure 8). The results of the straylight measurement are reported in §3.2.

Figure 8. Front view of the telescope & baffle with the black blankets set-up for the straylight test (Courtesy Airbus Defense&Space).

NISP

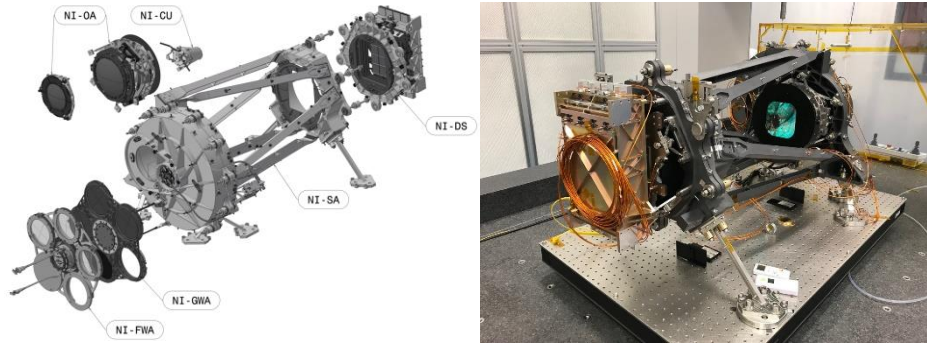All the different parts of the NISP were qualified and tested before being integrated (Figure 9).

Figure 9. (Left)Exploded view of the NISP instrument different parts; (Right)NISP Flight Model (FM) instrument during the detection unit integration.

Of particular interest are the detection unit (NI-DS in Figure 9) and the focusing optical system (NI-OA in Figure 9). The detectors went thorough qualification and characterization before integration in the NI-DS. The NI-OA have demonstrated outstanding performance at operational temperature (Figure 10) and the Point Spread Function (PSF) and WFE have been measured.
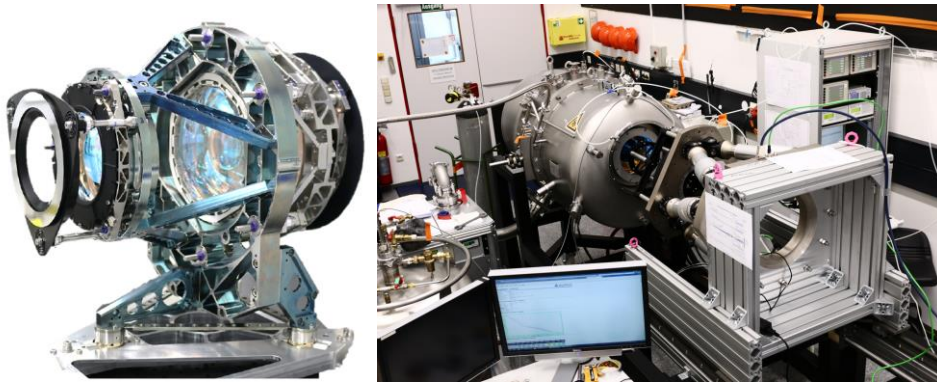

Figure 10. (Left)NI-OA part integrated in its dedicated mounting for testing in thermal-vacuum conditions; (Right) Test set-up for the NI-OA only.

Once the NISP parts qualified, the instrument was fully integrated and its performance also characterized in thermal-vacuum conditions at operational temperature[9]. The purpose of this test campaign was not only to verify the performance and the correct operation of the instrument as a whole but also to gather the necessary information for its alignment with the telescope. The most important information being the actual position of the instrument reference plane R_{NISP}[8] with respect to the reference frame R_u associated with the feet of the NISP bipods (Figure 11).
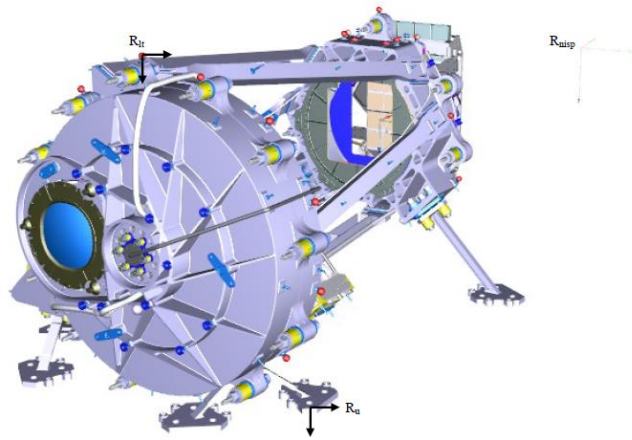
Figure 11. Definition of the NISP reference frames used for the alignment of the instrument with the telescope.

VIS

The VIS sub-elements as the Focal Plane Array (VIS-FPA) of CCDs, the Read-out Shutter Unit (VIS-RSU) and the Calibration Unit (VIS-CU) has been characterized and underwent a qualification program. The implementation of the VIS instrument in the PLM in shown in Figure 12.
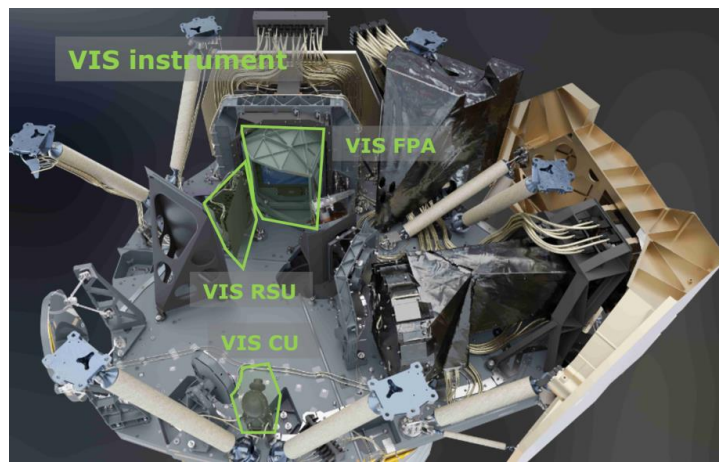

Figure 12. 3D view of the implementation of the VIS instrument elements in the PLM.

The main performance driving parameters of the VIS-FPA have been characterized in thermal-vacuum at operational temperature. In Figure 13 are shown the Quantum Efficiency (QE) and the ratio Gain/QE at λ=850nm as measured in thermal-vacuum conditions.
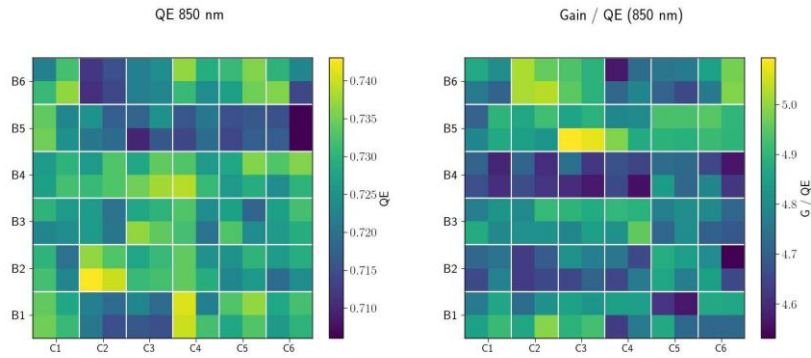
Figure 13. (Letf) QE map at λ=850nm; (right) ratio Gain vs QE at λ=850nm.

The small scale uniformity (over 100 pixels) of the VIS-CU illumination is also paramount to the final performance of the PLM. A dedicated characterization test has been devised and implemented. The area of illumination is scanned with a camera while the VIS-CU is placed within a thermal chamber (Figure 14). The information derived are the uniformity and also the size of the illuminated area provided by the VIS-CU lens.
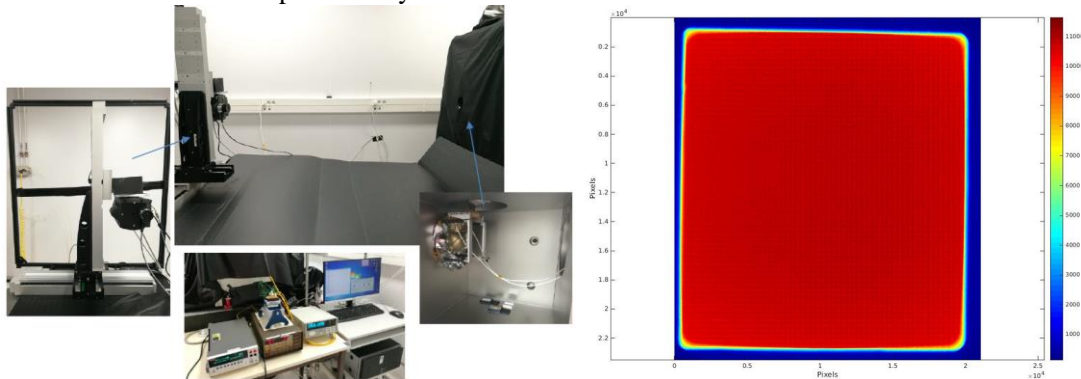

Figure 14. (Left) Test set-up for the VIS-CU irradiance area characterization; (right) irradiance map measured.

Test equipment

In addition of the payload elements, dedicated testing equipment's have been manufactured. As part of the future end to end thermal vacuum test a specially dedicated collimator (Figure 15) was developed delivered in 2019. Its purpose is to provide a high quality and stable wavefront to the telescope during optical testing with the instruments running at operational temperature.
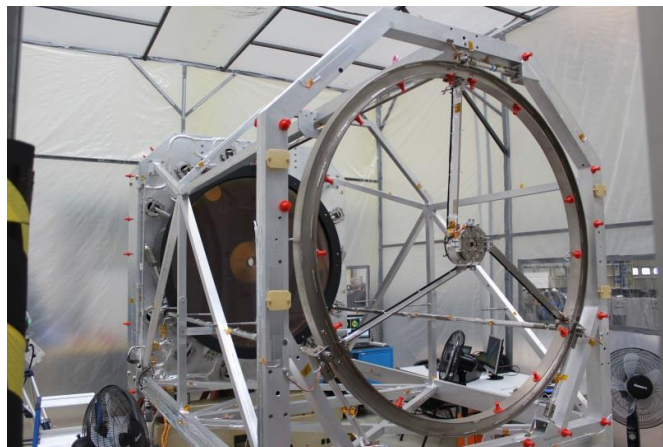

Figure 15. Front view of the collimator.

2.3 Development timeline

The PLM integration is currently on-going. The mechanical and electrical integration of the instruments in the PLM is completed. A thermal-vacuum test campaign of the PLM will be performed in 2021 with the finality to verify the correct functioning of the instruments after integration as well as optical testing and verification of optical alignment stability with the dedicated collimator. In addition, specific test are designed to collect data useful for the in-flight calibration. The delivery of the PLM to the prime Thales Alenia Space – Italia is planned for June 2021 for integration with the SVM. The environmental test campaign of the spacecraft will begin in late 2021, and the Flight Acceptance Review (FAR) will be held in July 2022.
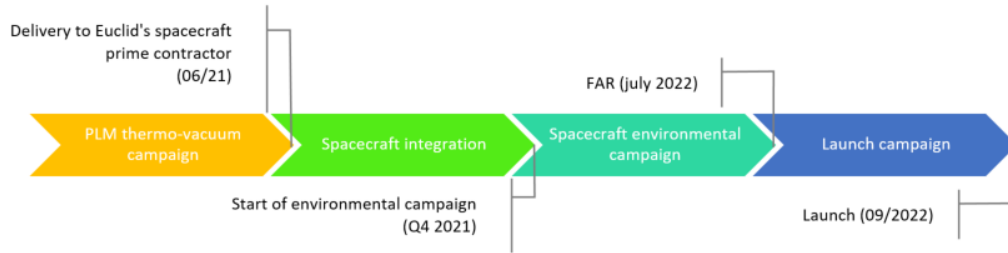

Figure 16. Overview of the spacecraft development timeline.

3. PERFORMANCE STATUS

3.1 Image quality

The image quality is quantified with specific metrics characterizing the Point Spread Function (PSF) of the end to end system. The metrics are the encircled energy at 50% (EE50) and 80% (EE80) for the NISP; the PSF Full Width at Half Maximum (FWHM), ellipticity (ϵ) and R^2 for the VIS. The latest two are specific metrics that determine systematic errors for the weak lensing experiment[10]. The end to end system PSF is the result of the convolution of various contributors along the chain of image acquisition namely: the telescope, the instruments (detectors and the optics for the NISP) and the spacecraft pointing jitter.

For the VIS instrument, the CCDs contribution to the system PSF is dominated by the brighter-fatter effect, which has been characterized on engineering models[11], and Charge Transfer Inefficiency (CTI). For the infrared detectors of the NISP the detectors' Inter-Pixel Capacitance (IPC)[12] is modelled by a 2×2 convolution kernel[13] applied to optical PSF of the telescope. For the flight detectors, the IPC was found to be less than 1%. In addition the optics of the NI-OA must be taken into account. For that purpose the wavefront delivered by the NISP optics are derived from the tolerances including manufacturing and alignment. The wavefront maps are then combined with the wavefront of the worst (WC) and typical (TC) telescope models generated with Monte-Carlo run. From there the PSFs of the combined system are calculated along with their associated metrics. The spacecraft pointing jitter worst case is determined by a Monte-Carlo from which a convolution matrix is derived and convolve with the instruments PSFs. Examples of PSFs including all contributor for the VIS are shown in Figure 17.
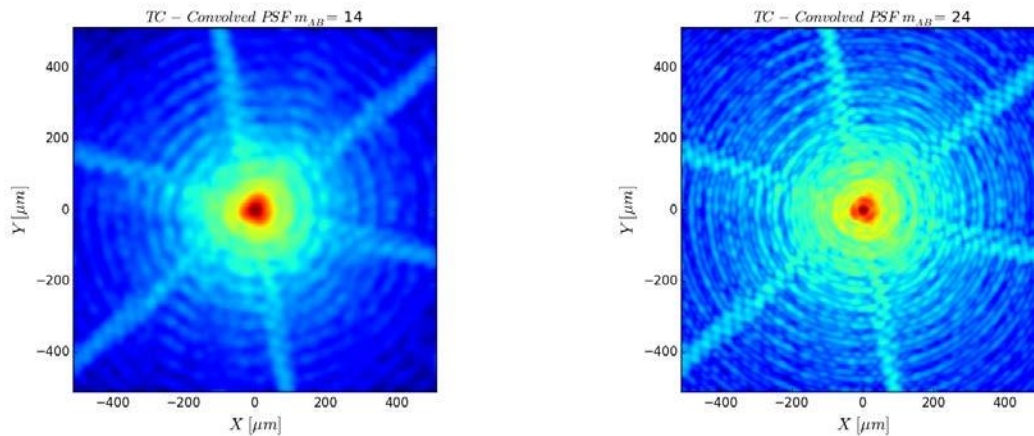
Figure 17. Examples of monochromatic PSFs at λ=800nm including the VIS instrument and spacecraft pointing jitter for two different object magnitude (or input flux at the telescope entrance pupil). (Left) Input flux is equivalent to a magnitude of 14; (right) input flux is equivalent to a magnitude of 24.

In Figure 17 the impact of the brighter-fatter is conspicuous. It results in the blurring of higher spatial frequencies for brighter objects. An additional degradation can be found in the thermal-mechanical constraints induced by the interface between the PLM and the SVM. An extensive Structural-Thermal-Optical-Performance[14] (STOP) analysis has been performed in order to determine the contribution of the thermal feedback from the SVM towards the PLM on the PSF metrics.

The degradation of the PSF metrics when combining all contributors can easily be seen in Figure 18 where is plotted the Full Width at Half Maximum (FWHM) end to end. It was found that the stability of the spacecraft pointing is a minor contributor to the PSF metrics.
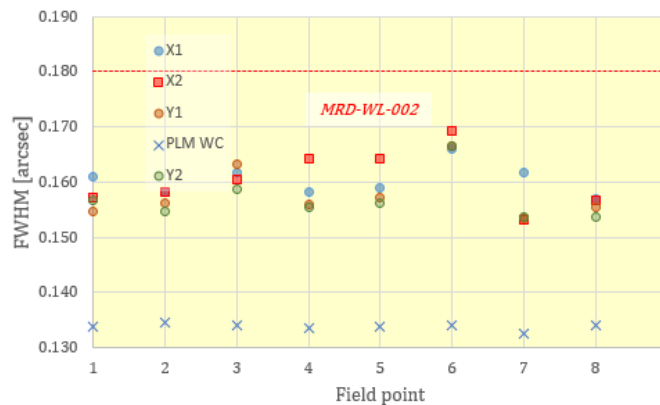

Figure 18. FWHM of VIS PSFs for the WC telescope model at λ=800nm for 9 field points in the VIS field of view. The crosses indicate the FWHM for the telescope alone. Each other points indicate the FWHM for different spacecraft jitter time series labelled X1, X2, Y1 and Y2. The red dashed line indicates the requirement (labelled MRD-WL-002) for the end to end FWHM.

A similar exercise has been performed for the NISP channel. The results for the WC telescope for the photometry mode of the NISP instrument is reported in Figure 19.
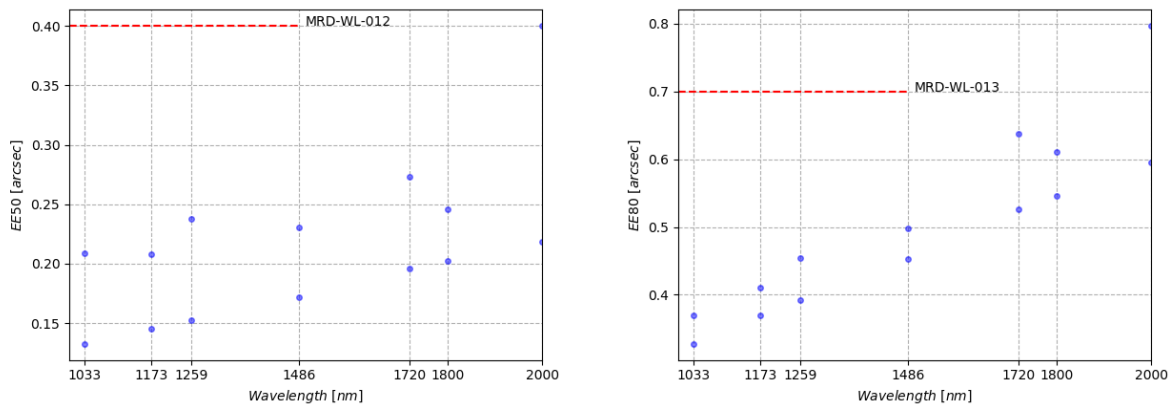
Figure 19. Mean and worst case encircled energies at 50% and 80% end to end at different wavelengths in the photometry mode of the NISP instrument. The red dashed line indicates the end to end requirement labelled MRD-WL-12/13.

3.2 Straylight

The straylight is specified by the Normalized Detector Irradiance(NDI)[15]. The NDI is defined as the ratio of the irradiance (power per unit area) at a specific point of the focal plane to the irradiance at the entrance pupil for an angular position of an observed punctual object. Extensive analyses of the straylight, of each instrument and of the telescope alone and for the entire system have been conducted[7] using the expected end of life particulate contamination. The NDI for each field point can be plotted in 2D radar plots (Figure 20). Each NDI plot is centered on the local PSF centroid, the NDI describing thus the distribution of the scattered energy around the PSF.
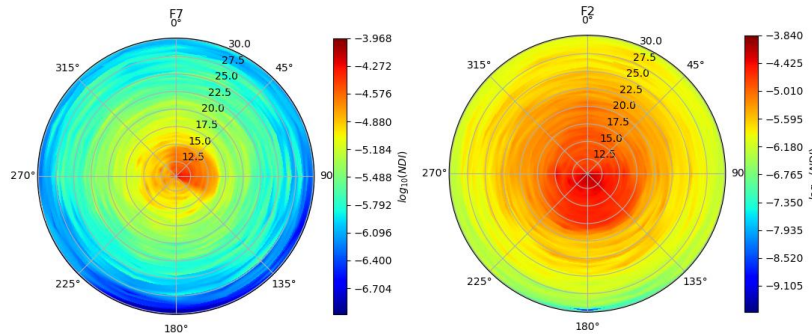

Figure 20. Examples of 2D NDI of the telescope alone calculated at one corner(left) and at the center(right) of the VIS field of view at λ=550nm. In the radar plots, the angular elevation of the source with respect to the spacecraft is along the radial coordinate while the azimuth of the source is along the polar angle coordinate.

From Figure 20 it can be inferred that the aspect of the NDI is changing across the field of view. The plotted NDIs for the elevation coordinates comprised between 0.03° and 0.3° (Figure 21) show clearly the contribution of the field stop of the telescope.
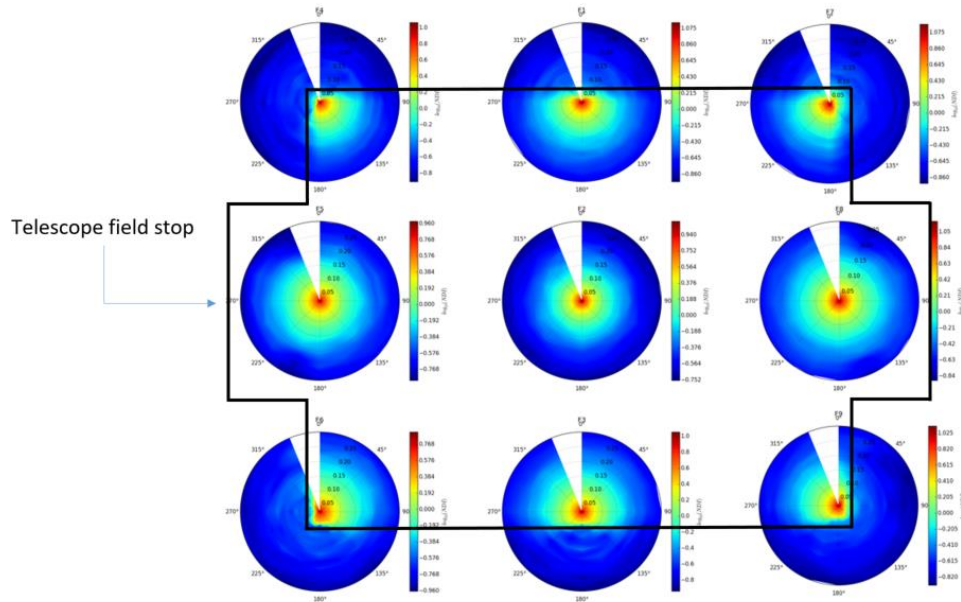
Figure 21. 2D NDI for 9 field positions in the VIS focal plane. The field F1, F3, F4, F6, F7 and F9 are located close to the edge of the VIS field of view. The telescope field stop shape is superposed to the plots to illustrate its effect on the NDI variation across the field of view.

The end to end NDI for the NISP in photometry mode is obtained by linearly summing the NDI of the NISP instrument alone with the NDI of the telescope (Figure 22). A end to end straylight analysis including all elements has been performed to validate the final results (Figure 22). A filtering effect of the NISP baffles seems to appear, the linear sum of the NDIs is thus a worst case.
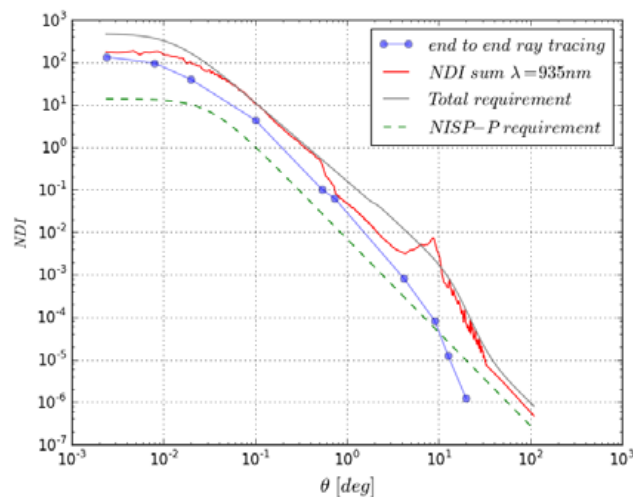

Figure 22. End to end straylight obtained by linear summation of the NDIs and by end to end analysis.

The spectroscopy mode required a characterisation of the Bi-directional Transmittance Distribution Function (BTDF) of the grism used in the instrument. The measured BRDF is integrated in the end to end straylight model and the straylight in the NISP focal plane is calculated (Figure 23).
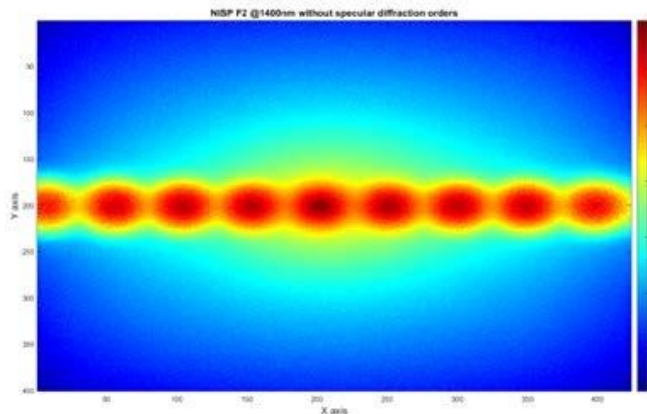
Figure 23. End to end straylight in the NISP focal plane at the center of the NISP field of view at λ=1400nm at 1 st diffraction order.

As for the photometry mode, each peak in Figure 23 is below the maximum allowed level.

The analysis is complemented by tests performed on the telescope as reported in §2.2. The NDI of the telescope has been measured (Figure 24) with a low level of particulate contamination on the mirrors and thus show very low levels of straylight close to the PSF core. Four the out-of-field straylight (starting at 1°) the level are below the specification but still close. However this is not expected to change with time as in this range of elevation the scattering on the structural parts is dominating.
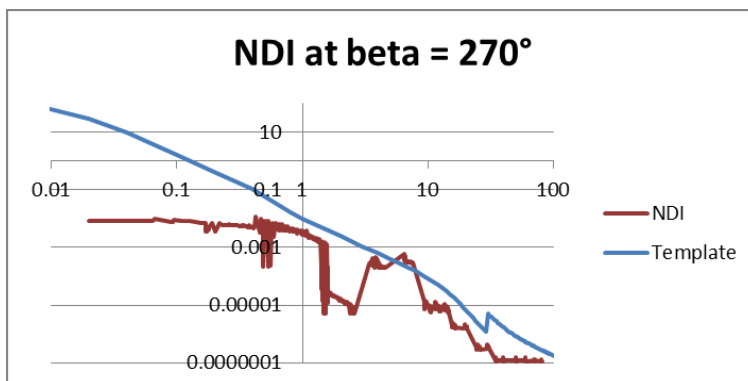

Figure 24. Telescope NDI in the VIS focal plane for an object at azimuth 270°.

3.3 Radiometric performance

The radiometric performance is defined in Signal to Noise Ratio (SNR) for the VIS and NISP. The SNR distribution in the sky can be derived, given a known distribution of galaxies with given spectra, once the NDI and the spectral throughput (Figure 25) of the PLM is established. For each field point, the straylight created by the zodiacal background is and the light others sources in the sky is calculated using the NDI function.

Taking into account all contributors, the SNR achieved for the VIS reaches 16 for an object of magnitude 24.5 which is larger than the specification.
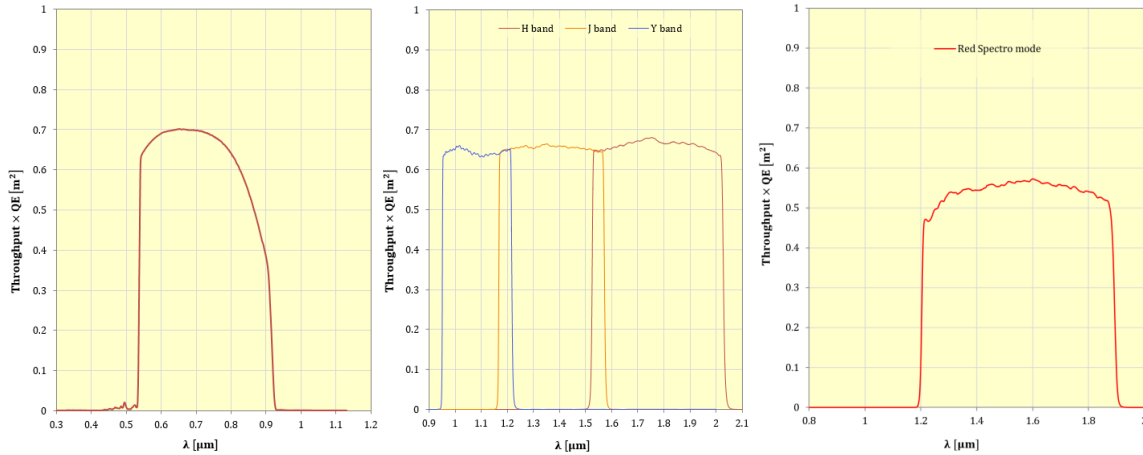
Figure 25. End to end PLM throughput including the particulate contamination: (Left) VIS; (middle) NISP photometry mode;(right) NISP spectroscopy mode diffraction order m=1.

With the same approach the SNR for both modes of the NISP is calculated (Figure 26). In both cases the SNR is higher than the minimum required SNR for the sensitivity flux defined .
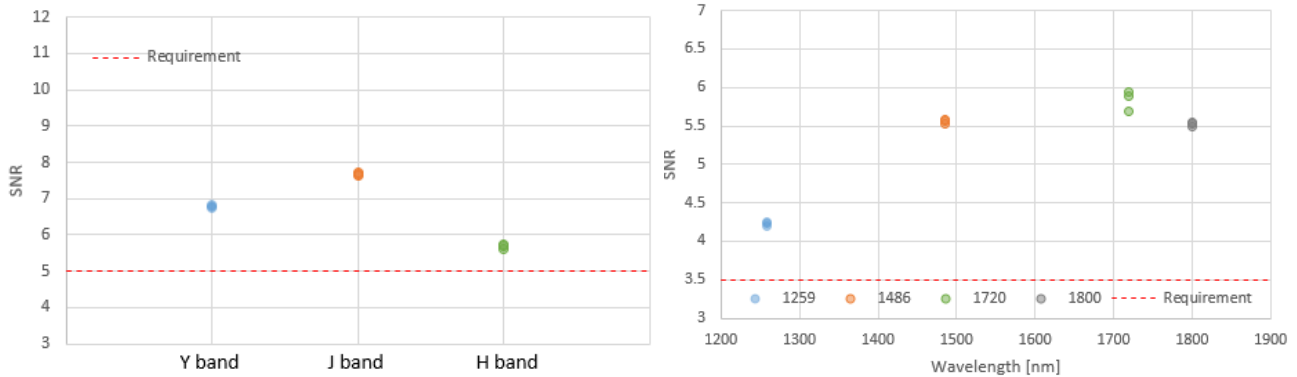

Figure 26. SNR results for the NISP: (Left) Photometry mode; (right) Spectroscopy mode.

3.4 Wavefront spectral dependence

It was verified that the di-electric coatings used on the optical elements of the telescope would have a significant impact on the PSF shape[16]. The dichroic having the larger beam footprint, its contribution is dominating the wavefront spectral dependence. A model describing this effect has been established and compared to measurements performed on a prototype of the dichroic. The results of simulations (Figure 27) clearly show a significant change of the wavefront error which needs to be accurately calibrated. A fourfold strategy is defined to mitigate this effect and ensure that the PLM provides the quality of data needed to meet the scientific objectives of the mission. The steps defined include:

1. Change the di-electric coating of the FOM3 to coated silver
2. A characterization of the flight dichroic
3. A validation of the coating model developed
4. The definition of an in-flight calibration strategy.

For the first point, ESA is funding the development of a specific test bench. The characterization will be made on a flight spare of the dichroic and will include the variation with the angle of incidence and the polarization. The characterization will be completed by 2022, in time for the commissioning and performance verification phase of the spacecraft after launch.
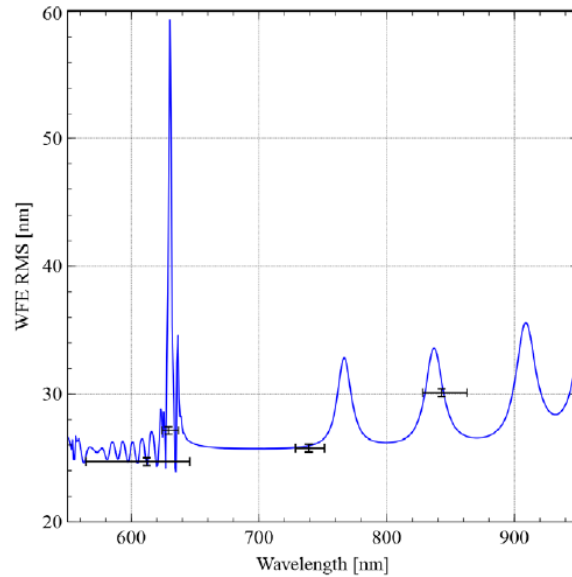
Figure 27. Wavefront error spectral dependence as modelled.

4. CONCLUSION

Despite the challenges encountered in the last months due to the current pandemic, the qualification and integration of all the different sub-systems of the Euclid spacecraft have been completed thanks to efforts of ESA's industrial and scientific partners. The testing of the SVM elements are showing good progress while the PLM has now completed its integration in order to be ready for the thermal-vacuum test campaign to be held in early 2021. This will be the next major step in the verification of the spacecraft.

The performance of the as-built PLM have been assessed during the Mission CDR. The compliance of the hardware to the scientific requirements despite its extremely demanding degree is met with some margins. A refinement of the performance (image quality) is on-going, including the latest information available on the as measured telescope components. In addition, an experimental characterization of the dichroic flight spare will be performed to gathered the necessary data for in-flight calibration of the spectral dependence of the wavefront error.

REFERENCES

[1] References ESA, "Euclid Mapping the geometry of the dark universe", ESA/SRE(2011)12, July 2011, http://sci.esa.int/euclid/48983-euclid-definition-study-report-esa-sre-2011-12/#.

[2] Cropper, M., Hoekstra, H., Kitching, T., Massey, R., Amiaux, J., Miller, L., Mellier, Y., Rhodes, J., Rowe, B., Pires, S., Saxton, C. and Scaramella, R., "Defining a weak lensing experiment in space," Monthly Notices of the Royal Astronomical Society **431**(4), 3103–3126 (2013).

[3] Racca, G. D., Laureijs, R., Stagnaro, L., Salvignol, J.-C., Alvarez, J. L., Criado, G. S., Venancio, L. G., Short, A., Strada, P., Bönke, T., Colombo, C., Calvi, A., Maiorano, E., Piersanti, O., Prezelus, S., Rosato, P., Pinel, J., Rozemeijer, H., Lesna, V., et al., "The Euclid mission design," Space Telescopes and Instrumentation 2016: Optical, Infrared, and Millimeter Wave **9904**, 99040O, International Society for Optics and Photonics (2016).

[4] Cropper, M., Pottinger, S., Azzollini, R., Szafraniec, M., Awan, S., Mellier, Y., Berthé, M., Martignac, J., Cara, C., Giorgio, A.-M. D., Sciortino, A., Bozzo, E., Genolet, L., Philippon, A., Hailey, M., Hunt, T., Swindells, I., Holland, A., Gow, J., et al., "VIS: the visible imager for Euclid," Space Telescopes and Instrumentation 2018: Optical, Infrared, and Millimeter Wave **10698**, 1069828, International Society for Optics and Photonics (2018).

[5] Maciaszek, T., Ealet, A., Jahnke, K., Prieto, E., Barbier, R., Mellier, Y., Beaumont, F., Bon, W., Bonnefoi, A., Carle, M., Caillat, A., Costille, A., Dormoy, D., Ducret, F., Fabron, C., Febvre, A., Foulon, B., Garcia, J., Gimenez, J.-L., et al., "Euclid Near Infrared Spectrometer and Photometer instrument concept and first test results obtained for different breadboards models at the end of phase C," Space Telescopes and Instrumentation 2016: Optical, Infrared, and Millimeter Wave **9904**, 99040T, International Society for Optics and Photonics (2016).

[6] F. Grupp, E. Prieto, N. Geis, A. Bode, R. Katterloher, R. Grange, V. Junk, and R. Bender, "The optical baseline concept of the NISP near infrared spectrometer and photometer on board of the ESA/EUCLID satellite", Proc. SPIE 8442, p. 84420X–84420X–11 (2012).

[7] Venancio, L. M. G., Pachot, C., Carminati, L., Alvarez, J. L., Amiaux, J., Prieto, E., Bonino, L., Salvignol, J.-C., Short, A., Boenke, T., Strada, P. and Laureijs, R., "Euclid end-to-end straylight performance assessment," Space Telescopes and Instrumentation 2016: Optical, Infrared, and Millimeter Wave **9904**, 99040P, International Society for Optics and Photonics (2016).

[8] A. Costille; M. Carle; C. Fabron; E. Prieto; F. Beaumont; et al, "How to test NISP instrument for EUCLID mission in laboratory," Proc. SPIE 9904, Space Telescopes and Instrumentation 2016: Optical, Infrared, and Millimeter Wave, 9904-95 (2016).

[9] Costille, A., Carle, M., Prieto, E., Pons, M., Fabron, C., Andersen, M. I., Sorensen, A. N., Jensen, N. C., Pedersen, S. M. and Maciaszek, T., "Testing NISP instrument on ground," International Conference on Space Optics — ICSO 2018 **11180**, 111807L, International Society for Optics and Photonics (2019).

[10] Venancio, L. M. G., Laureijs, R., Lorenzo, J., Salvignol, J. C., Short, A., Strada, P., Vavrek, R., Vaillon, L., Gennaro, C., Amiaux, J. and Prieto, É., "Euclid payload module: telescope characteristics and technical challenges," Space Telescopes and Instrumentation 2014: Optical, Infrared, and Millimeter Wave **9143**, 91430I, International Society for Optics and Photonics (2014).

[11] Niemi, S.-M., Cropper, M., Szafraniec, M. and Kitching, T., "Measuring a charge-coupled device point spread function," Exp Astron **39**(2), 207–231 (2015).

[12] Moore, A. C., Ninkov, Z. and Forrest, W. J., "Interpixel capacitance in nondestructive focal plane arrays," presented at Optical Science and Technology, SPIE's 48th Annual Meeting, 12 January 2004, San Diego, California, USA, 204.

[13] McCullough, P., "Inter-pixel capacitance: prospects for deconvolution.", STScI Instrument Science report WFC3 2008-26 (2008).

[14] Baumer, S., "Beyond Tolerance Aanalysis - Structural Thermal Optical Performance Analysis," Optical Design and Fabrication 2017 (Freeform, IODC, OFT) (2017), paper ITu1A.7, ITu1A.7, Optical Society of America (2017).

[15] Pierre Y. Bely, [The design and construction of large optical telescopes], Astronomy & Astrophysics library, Springer Verlag, New-York, p.192 (2003).

[16] Venancio, L. M. G., Carminati, L., Alvarez, J. L., Amiaux, J., Bonino, L., Salvignol, J.-C., Vavrek, R., Laureijs, R., Short, A., Boenke, T. and Strada, P., "Coating induced phase shift and impact on Euclid imaging performance," Space Telescopes and Instrumentation 2016: Optical, Infrared, and Millimeter Wave **9904**, 99040V, International Society for Optics and Photonics (2016).